RAPID COMMUNICATION

Plasma-enhanced atomic-layer-deposited MoO$_x$ emitters for silicon heterojunction solar cells

Johannes Ziegler[1] · Mathias Mews[3] · Kai Kaufmann[4,5] · Thomas Schneider[1] ·
Alexander N. Sprafke[1] · Lars Korte[3] · Ralf B. Wehrspohn [1,2]

Abstract A method for the deposition of molybdenum oxide (MoO$_x$) with high growth rates at temperatures below 200 °C based on plasma-enhanced atomic layer deposition is presented. The stoichiometry of the over-stoichiometric MoO$_x$ films can be adjusted by the plasma parameters. First results of these layers acting as hole-selective contacts in silicon heterojunction solar cells are presented and discussed.

1 Introduction

Its spectrally broad transparency and high work function make evaporated molybdenum oxide (MoO$_x$) a promising candidate for substituting amorphous silicon emitter in silicon heterojunction (SHJ) solar cells [1]. Thus, the replacement of the p-doped amorphous silicon emitter by higher band gap materials like MoO$_x$ can lead to a gain in the photocurrent of such cells [2, 3]. However, a thin intrinsic amorphous silicon ((i)a-Si:H) layer between the oxide and the crystalline silicon (c-Si) is still needed to improve the poor surface passivation quality of the oxide and to fully benefit of the MoO$_x$-induced high open-circuit voltage (V_{OC}) [3].

Although the hole-selective conductivity mechanism through the MoO$_x$/(i)a-Si:H/(n)c-Si stack is not fully understood in detail, it is influenced by the defect state density in the MoO$_x$ as well as the MoO$_x$ layer thickness itself [3, 4].

For depositing very thin (<10 nm) conformal oxides on structured silicon surfaces, atomic layer deposition (ALD) is due to its reaction-limited growth process an ideal candidate [5]. Thermal ALD recipes for MoO$_x$ are recently reported by different groups, but up to now none of these MoO$_x$ layers are tested as emitter alternative in SHJ solar cells [6–8].

In this work, we introduce an alternative new plasma-enhanced atomic layer deposition (PE-ALD) process for MoO$_x$ layers. Influences of the process conditions on the stoichiometry of these layers as well as their performance on cell level are shown.

2 Experimental

The MoO$_x$ deposition was carried out by a PE-ALD process in a FlexAL ALD reactor (Oxford instruments) with inductively coupled plasma source. Before starting a deposition, the reactor chamber is pumped to a base pressure below 0.7 mPa and the substrate is heated to 180 °C. Due to the low vapor pressure of the used liquid Mo precursor (NtBu)$_2$(NMe$_2$)$_2$Mo, the source is heated to 50 °C and transported to the reactor chamber by Ar gas (step 1). After the first precursor dose, the reactor chamber is purged

✉ Johannes Ziegler
johannes.ziegler@physik.uni-halle.de

[1] μMD Group, Institute of Physics, Martin-Luther-University Halle-Wittenberg, Heinrich-Damerow-Strasse 4, 06120 Halle, Germany

[2] Fraunhofer Institute for Mechanics of Materials IWM Halle, Walter-Hülse-Str. 1, 06120 Halle, Germany

[3] Institute for Silicon-Photovoltaics, Helmholtz-Zentrum Berlin für Materialien und Energie GmbH, Kekuléstr. 5, 12489 Berlin, Germany

[4] Fraunhofer Center for Silicon Photovoltaics CSP, Otto-Eifeld-Strasse 12, 06120 Halle, Germany

[5] Hochschule Anhalt Köthen, University of Applied Sciences, Bernburger Str. 55, 06966 Köthen, Germany

by Ar only (step 2), while later in the purge step the Ar flow through the ICP source is changed to O_2 to get a stable O_2 flow trough the plasma source (step 3). In next step (step 4), O_2 plasma is burned over the substrate with a plasma power of 300 W. The last step (step 5) in the cycle is done by flowing O_2 through the ICP source for the 1 s (1-second O_2 plasma) and the two second O_2 (2-second O_2 plasma) plasma processes (Figs. 1, 2). The minimal reactor pressure is set to 2 Pa. The upper limit of each step of the different processes is given in the process cycle overview (see Figs. 1, 2, 3). The PE-ALD plasma step duration is varied between 1 s (Fig. 1) and 2 s (Fig. 2). Additionally, the influence of an Ar plasma on the MoO_x layers is tested by inserting a six-second Ar plasma step with 300 W plasma power (2-second O_2 plasma and Ar) (compare Fig. 3).

The thicknesses and growth per cycle (GPC) of the produced MoO_x layers on silicon substrate are measured by spectral ellipsometry using a Tauc–Lorentz model combined with an Gauss oscillator to model sub-band-gap absorption if necessary [9]. X-ray photoelectrons spectra of the as-deposited MoO_x layers are measured by a Kratos Axis Ultra photoelectron spectrometer (X-ray source Al $E_{K_\alpha} = 1486.7$ eV).
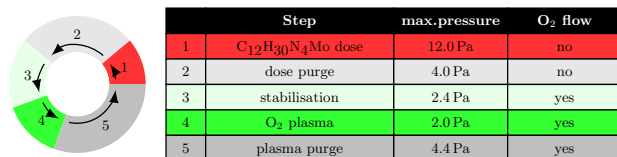
duration one cycle 7.2 s

	Step	max.pressure	O_2 flow
1	$C_{12}H_{30}N_4Mo$ dose	12.0 Pa	no
2	dose purge	4.0 Pa	no
3	stabilisation	2.4 Pa	yes
4	O_2 plasma	2.0 Pa	yes
5	plasma purge	4.4 Pa	yes

Fig. 1 Schema PE-ALD MoO_x process "1-second O_2 plasma"

duration one cycle 8.2 s

	Step	max.pressure	O_2 flow
1	$C_{12}H_{30}N_4Mo$ dose	16.0 Pa	no
2	dose purge	4.9 Pa	no
3	stabilisation	2.6 Pa	yes
4	O_2 plasma	2.0 Pa	yes
5	plasma purge	6.4 Pa	yes
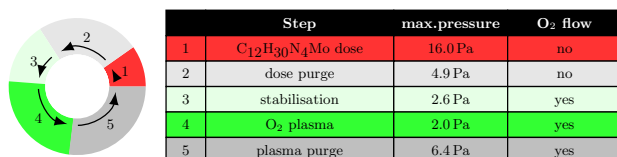
Fig. 2 Schema PE-ALD MoO_x process "2-second O_2 plasma"

duration one cycle 13.2 s

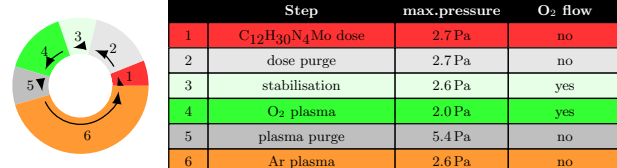|	Step	max.pressure	O_2 flow
1	$C_{12}H_{30}N_4Mo$ dose	2.7 Pa	no
2	dose purge	2.7 Pa	no
3	stabilisation	2.6 Pa	yes
4	O_2 plasma	2.0 Pa	yes
5	plasma purge	5.4 Pa	no
6	Ar plasma	2.6 Pa	no

Fig. 3 Schema PE-ALD MoO_x process "2-second O_2 and Ar plasma"

For the solar cell preparation, polished float-zone-grown phosphorous-doped (100) silicon wafers with a resistivity of 1–5 Ωcm were used. The wafers were cleaned using the RCA process and dipped in diluted hydrofluoric acid (2 min, 1 % vol.) prior to amorphous silicon depositions, and 5-nm intrinsic amorphous silicon was deposited at the front side of the wafers, and a stack of 4-nm intrinsic and 8-nm phosphorous-doped amorphous silicon was deposited on the back side.

Amorphous silicon layers were deposited by plasma-enhanced chemical vapor deposition. The intrinsic amorphous silicon layers were deposited using an excitation frequency of 13.56 MHz and a power density of 20 mW/cm^2. The deposition temperature was 170 °C, the pressure was 0.5 mbar, the distance between electrode and substrate on the grounded electrode was 3 cm, and the process gas consisted of pure silane. The intrinsic layers were exposed to a hydrogen plasma treatment [10] in the same reactor at 1 mbar, an electrode substrate distance of 5 cm and a plasma power density of 60 mW/cm^2.

Phosphorous-doped amorphous silicon was grown in a reactor with 60 MHz excitation, at 0.5 mbar, 195 °C, with an electrode distance of 2.3 cm, at plasma power density of 20 mW/cm^2 with a gas-phase doping of 2000 ppm provided by mixing phosphine diluted at 1 % in hydrogen with silane.

Directly after a 1-min dip in 1 %vol. diluted Hf, to remove an potential native oxide from the amorphous silicon, 10- and 20-nm-thick molybdenum oxide layers have been deposited by the introduced PE-ALD processes with varying plasma steps on the front side of the wafers. Following the molybdenum oxide depositions, indium tin oxide (ITO) was sputtered onto the samples. The ITO layers were RF-sputtered from a ceramic target at a pressure of 6 mbar, a sputtering power of 70 W, a voltage of about 165 V and a gas flow of 40 sccm. The sputter gas consisted of argon with 0.2 % oxygen for the front side ITO and 0.5 % oxygen for the back side layer. The thickness of the front side ITO is about 80 nm, while about 150 nm was deposited on the back side. Since the layers were deposited at room temperature, a two minute post-deposition anneal at 200 °C was conducted.

Metal contacts were applied by thermal evaporation of titanium silver stacks. Ten nanometer of titanium was deposited as an adhesion layer, and 500 nm of silver was added on the back side and 1500 nm on the front side. The front side evaporation was conducted through a shadow mask. Afterwards, the solar cell area of 1 cm^2 was defined by photolithography and HCl etching of the ITO layer on the front side.

Photoconductance decay measurements were conducted using a Sinton Instruments system to measure the minority

carrier lifetime of the wafers in between different process steps [11]. Bright IV of the solar cells was measured using a class c sun simulator.

3 Results and discussion

In Fig. 4, the MoO$_x$ film thickness determined by spectral ellipsometry, plotted over the number of performed ALD cycles for the 1-second and 2-second O$_2$ plasma processes, is shown. A very similar linear increase in layer thickness with number of cycles is found for both processes. The relatively high growth rate per cycle of $0.06(5) \pm 0.008$ nm for both O$_2$ plasma durations indicates that oxygen saturation is reached at a plasma power of 300 W within 1 s. This high growth rate at 180 °C is one main benefit compared to the thermal ALD MoO$_x$ process reported by Bertuch et al. [8], who use the same Mo precursor but ozone as oxidant. For the thermal ALD MoO$_x$ process at temperatures below 200 °C, growth rate per cycle below 0.03 nm is reported. By PE-ALD, the activation energy can be delivered by the oxygen reactants from O$_2$ plasma. This enables higher growth rates especially for lower deposition temperatures. The growth rates are not significantly influenced by longer purge times or by the integration of an additional Ar plasma step in the cycle, like its done on the process 2-second O$_2$ and 6-second Ar plasma (Fig. 3) (not shown).

The optical parameters, estimated from the ellipsometry data of the different MoO$_x$ layers, are slightly affected by the duration of the plasma step (compare Fig. 5). While the 2-second O$_2$ plasma process shows no sub-band-gap absorption, the additional argon plasma step

leads to small, wide sub-band-gap absorption in the MoO$_x$ layers the. For 1-second O$_2$ plasma duration, the sub-band-gap absorption is more pronounced and less wide (Fig. 5).

X-ray photoelectron spectroscopy (XPS) was used to identify the core level binding energies and oxidation states of the MoO$_x$ layers. The spectra of the films on silicon show characteristic peaks for the oxygen molybdenum. Beside a small carbon peak from surface contamination, no additional peaks can be found in the survey spectra (not shown). In Fig. 6, very similar spectra for all processes can be found in the Mo3d doublet region. Two peaks are observed at 232.5 and 235.6 eV, which correspond to the Mo 3$d_{5/2}$ and Mo 3$d_{3/2}$, respectively. This values are
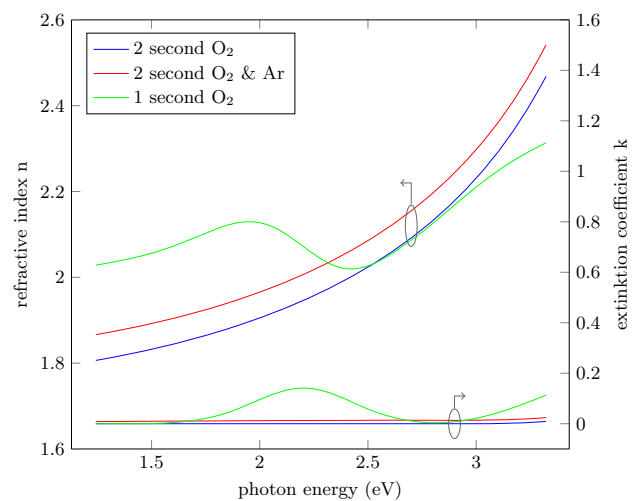
Fig. 5 Refractive index n and extinction coefficient k of the produced MoO$_x$ layer as determined from spectroscopic ellipsometry
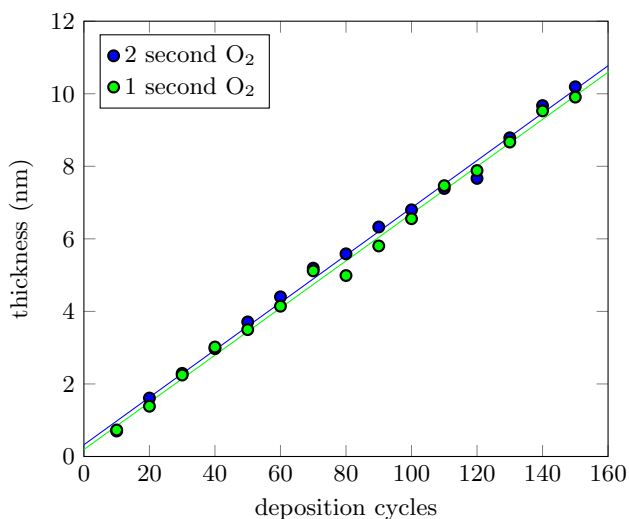
Fig. 4 MoO$_x$ thickness measured by spectral ellipsometry data plotted versus the number of ALD cycles
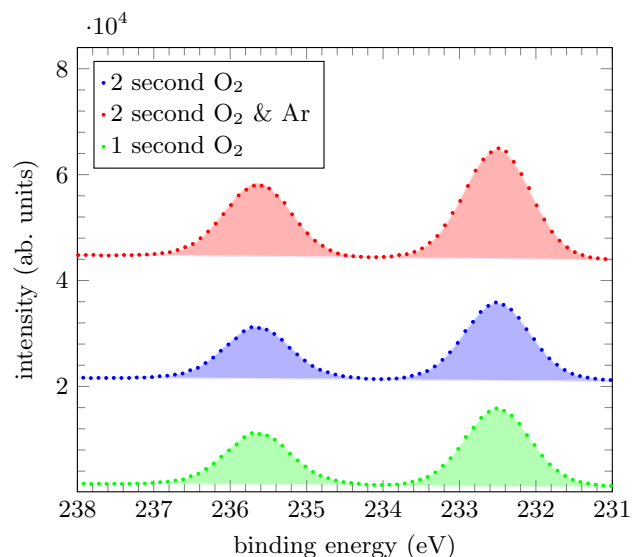
Fig. 6 XPS spectra of the Mo3d doublet of MoO$_x$ films grown in PE-ALD processes with varying plasma step

consistent with reported values for the Mo oxidation state of 6+ in literature (232.3–232.6 eV for the Mo $3d_{5/2}$ and 235.4–235.7 eV for the Mo $3d_{3/2}$ [4, 6, 8, 12]).
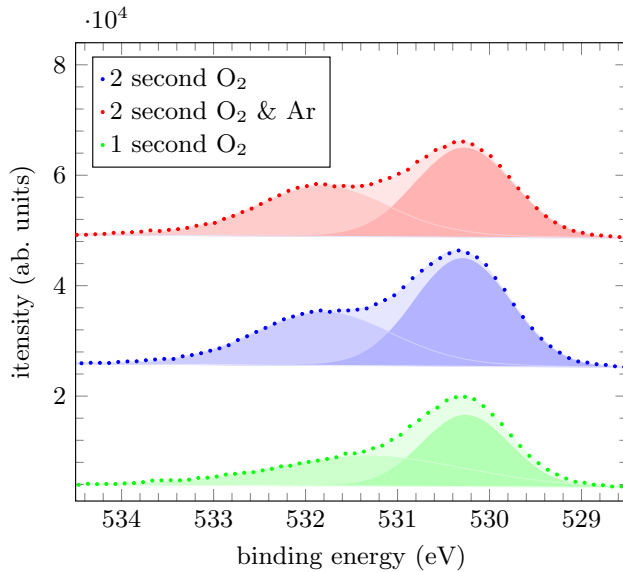

Fig. 7 XPS spectra of O 1s energy region of MoO_x films grown in PE-ALD processes with varying plasma step

A clear difference can be found in the O 1s energy region in Fig. 7. While all measurements show a similar O 1s peak at 530.3 eV, a second oxygen-related peak at higher binding energies can be found in the spectra. In the 1-second O_2 process spectrum, this peak at 531.3 eV is less pronounced, compared with the spectra of 2-second O_2 processes, in which this peak is located at slightly higher binding energies at 531.8 eV. Choi and coauthors [12] assign a very similar peak in molybdenum oxide to strongly absorbed oxygen as O^-, HO^- or H_2O. Although we cannot exclude that this peak is formed by adsorbed air moisture in the layers, as samples were not transferred in vacuo to the spectrometer. It is very likely that this difference is process related, in particular because the samples have been produced after each other and transferred together. It seems plausible that a longer oxygen plasma step leads to a higher content of strongly absorbed oxygen in the MoO_x layers itself. However, a stoichiometry analysis of the measured XPS spectra shows over-stoichiometric ($x > 3$) MoO_x for all produced layers. While the O to Mo proportion $x = 3.15$ is estimated for the 1-second O_2 layer, a higher oxygen content is measured for 2-second O_2 plasma processes $x = 3.62$ without and $x = 3.55$ with Ar plasma step.

Fig. 8 Solar cell results plotted versus MoO_x processes for 10- and 20-nm-thick oxide layers
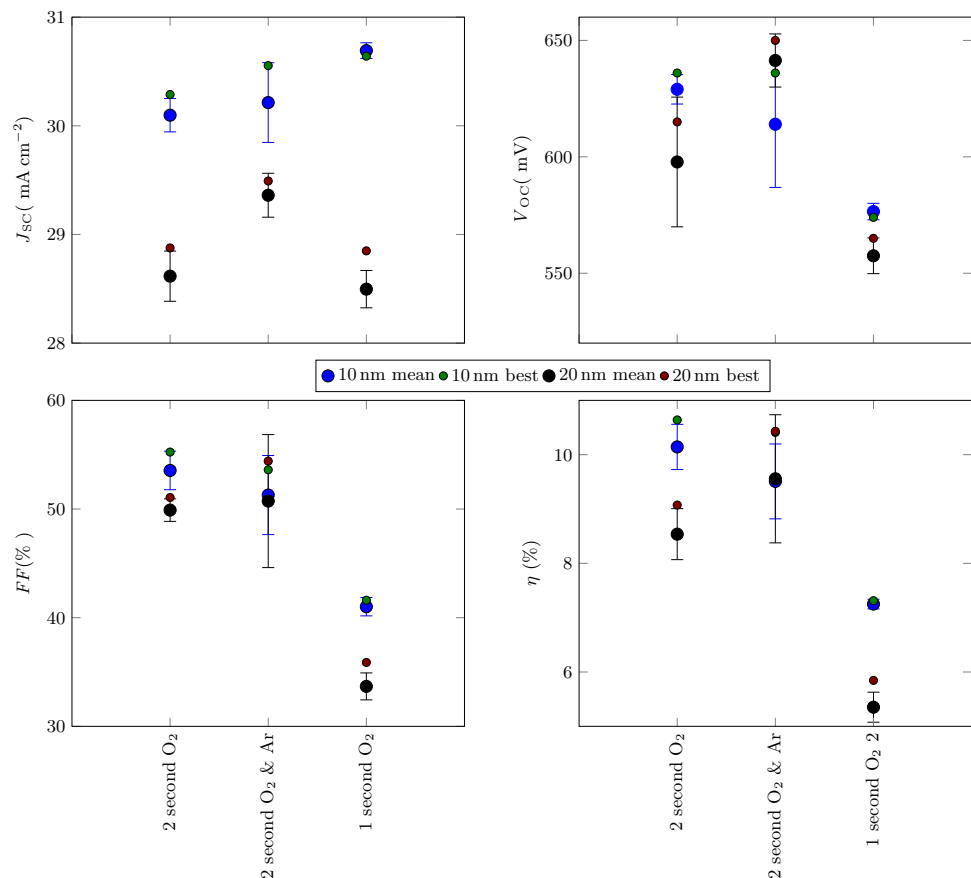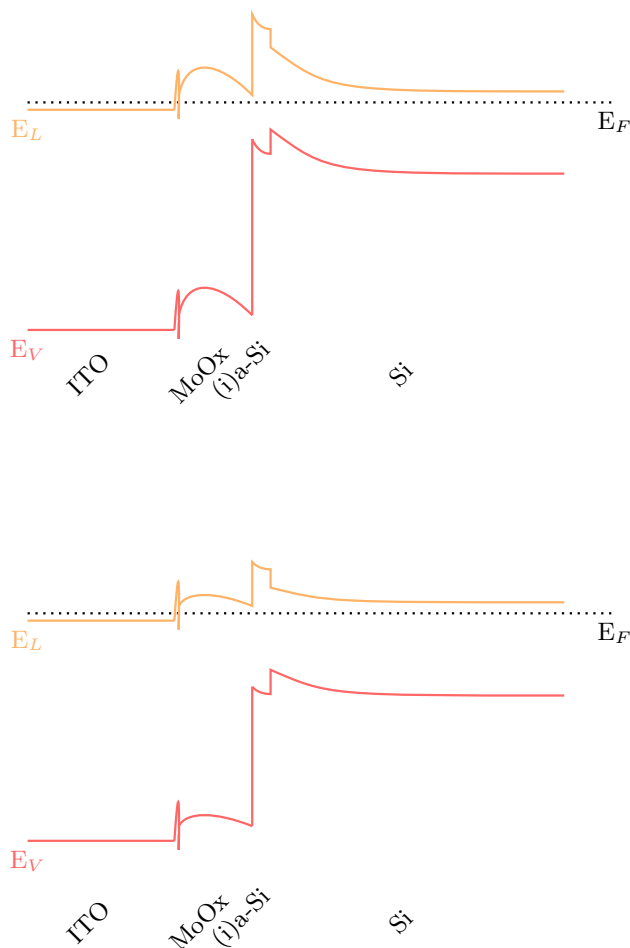
Fig. 9 Sketch illustrating differences in MoO$_x$ induced dark band bending above: high work function MoO$_x$, below: low work function MoO$_x$

Fig. 10 Bright IV curves of SHJ cells with 10 nm MoO$_x$

The performance of the different MoO$_x$ processes is tested for 10- and 20-nm-thick oxide layers in SHJ solar cells. The cell results (compare Fig. 8) show significant differences mainly in the open-circuit voltage. While the oxides grown in the 2-second O$_2$ plasma processes reach best V_{OC} values above 610 mV up to 650 mV, the best V_{OC} values reach by the oxides grown in the 1-second O$_2$ plasma processes are below 580 mV. It is worth to mention that the low open-circuit voltages in these cells are not limited by enhanced surface recombination. From lifetime measurements of the samples after ITO sputtering and post-anneal (not shown), a quasi-Fermi level splitting at 1 sun (often called implied V_{OC}) well above 700 mV could be measured for all samples. Both processes without Ar plasma step tend to slightly lower open-circuit voltages for thicker oxide layer. Cells with MoO$_x$ layers grown in a process with Ar plasma step show an opposite trend.

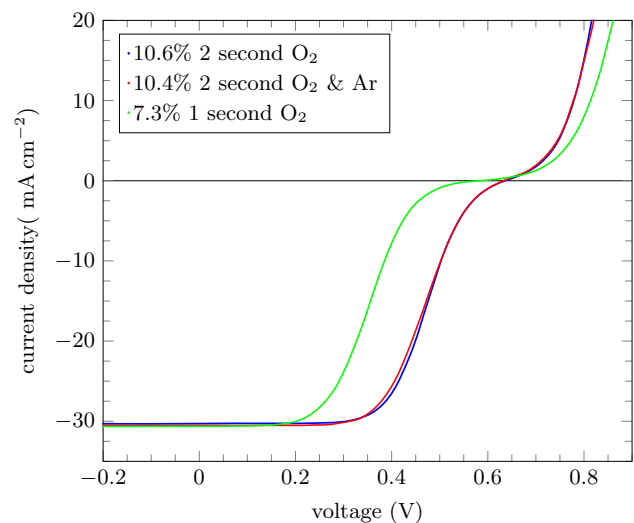The parasitic absorption in the thin oxides is not the only optical loss, shadowing of the ITO itself, as well as differences in the reflection of the front side stacks are also limiting the current. Therefore, the cells with thin (10 nm) oxide layers show very similar currents. A loss in current by doubling the oxide thickness can be seen in all produced cells. As expected the 1-s O$_2$ plasma processed MoO$_x$ layers show the highest optical lose, by doubling the layer thickness, above 1.3 mA cm^{-2}. Although the extinction coefficient, determined by spectral ellipsometry on as-deposited oxide layers, is slightly higher for the MoO$_x$ process with Ar plasma step, the short-circuit currents do not reflect such tendencies. This could indicate that the ITO sputtering step and the post-deposition anneal determine the optical properties of the MoO$_x$ layers. The fill factors and efficiencies of all cells are limited by differently strongly pronounced s-shape in the bright IV curves (compare Figs. 10, 11). Bataglia et al. [3] have reported similar "s-shape" feature, more pronounced for thicker evaporate MoO$_x$ layers of SHJ solar cells with MoO$_x$ emitter. Same tendencies can be found here for cells with MoO$_x$ layers grown in PE-ALD process without additional Ar plasma step. One possible reason for such shape could be the existence of a large barrier for hole transport in SHJ solar cells with sufficient front surface passivation [13]. At first sight, it seems plausible to assume that an insufficient hole transport through the MoO$_x$ layers itself is the dominating part of such barrier in the produced cells. The decrease in fill factor for thicker oxide layer seems to support this idea. Anyhow, MoO$_x$ layers grown in PE-ALD process with additional Ar plasma step do not show such dependency. On the other hand, the valence band offset on the a-Si:H/c-Si interface could be the dominating part of the barrier, if a tunneling process of holes through this offset is dominating the current a wider barrier leads to a more pronounced s-shape. The width of such barrier is
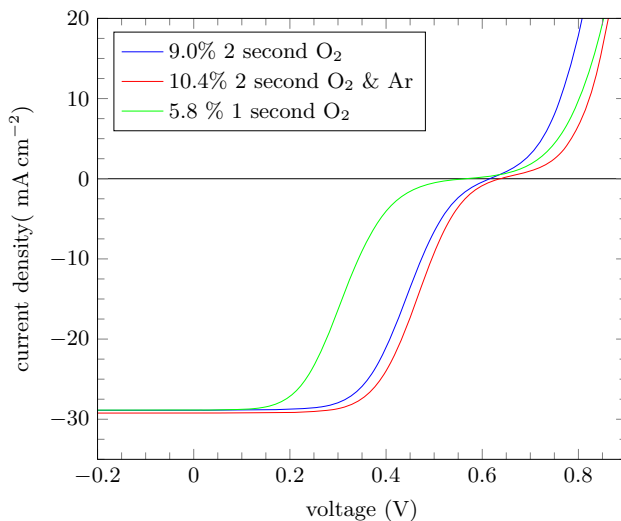
Fig. 11 Bright IV curves of SHJ cells with 20 nm MoO$_x$

working point dependent and directly influenced by the band bending. A lower work function of the MoO$_x$ would introduce a lower dark band bending in the c-Si (see schematic sketch in Fig. 9).

Therefore, a lower open-circuit voltage, and as well a more pronounced "s-shape" can be expected. In total, it leads to a significant loss in fill factor and efficiency.

It is known that work function in sub-stoichiometric molybdenum oxide ($x < 3$) decrease by the removal of oxygen [14]. Although all as-deposited oxides are over-stoichiometric, we speculate that the ITO sputter step and the post-deposition anneal can reduce the oxygen content in the MoO$_x$ layers during the cell process. It might be somehow plausible that after these reductions the MoO$_x$ layers with initial less oxygen still have a lower content and therefore a lower work function compared to layers with higher initial oxygen content. Such an effect would explain the high decrease in V_{OC} and fill factor seen in cells with MoO$_x$ layers grown the 1-second O$_2$ PE-ALD process, with lower initial oxygen content.

4 Conclusions

A new PE-ALD process for the deposition of MoO$_x$ with high growth rate at temperatures below 200 °C has been presented. XPS measurements show that the stoichiometry of the grown oxides can be influenced by the duration of the oxidizing plasma step. In a first experiment, the integration of these MoO$_x$ layers as alternative emitters in SHJ solar cells are tested with efficiencies above 10 %. A strong

influence of initial stoichiometry on the open-circuit voltage and on cell performance can be reported. The best cells have a 10-nm MoO$_x$ layer and a 2-second oxygen plasma step.

References

1. C. Battaglia, X. Yin, M. Zheng, I.D. Sharp, T. Chen, S. McDonnell, A. Azcatl, C. Carraro, B. Ma, R. Maboudian, R.M. Wallace, A. Javey, Nano Lett. **14**(2), 967 (2014). doi:10.1021/nl404389u
2. T. Mueller, S. Schwertheim, M. Scherff, W.R. Fahrner, Appl. Phys. Lett. **92**(3), 033504 (2008). doi:10.1063/1.2837192. http://scitation.aip.org/content/aip/journal/apl/92/3/10.1063/1.2837192
3. C. Battaglia, S.M. de Nicols, S. De Wolf, X. Yin, M. Zheng, C. Ballif, A. Javey, Appl. Phys. Lett. **104**(11), 113902 (2014). doi:10.1063/1.4868880. http://scitation.aip.org/content/aip/journal/apl/104/11/10.1063/1.4868880
4. M.T. Greiner, L. Chai, M.G. Helander, W.M. Tang, Z.H. Lu, Adv. Funct. Mater. **23**(2), 215 (2013). doi:10.1002/adfm.201200993
5. M. Otto, M. Kroll, T. Kasebier, R. Salzer, A. Tunnermann, R.B. Wehrspohn, Appl. Phys. Lett. **100**(19), 191603 (2012). doi:10.1063/1.4714546. http://link.aip.org/link/?APL/100/191603/1
6. M. Diskus, O. Nilsen, H. Fjellvag, J. Mater. Chem. **21**, 705 (2011). doi:10.1039/C0JM01099E
7. Y.C. Tseng, A.U. Mane, J.W. Elam, S.B. Darling, Solar Energy Mater. Solar Cells **99**(0), 235 (2012). doi:10.1016/j.solmat.2011.12.004. http://www.sciencedirect.com/science/article/pii/S0927024811006854. 9th International Meeting on Electrochromism
8. A. Bertuch, G. Sundaram, M. Saly, D. Moser, R. Kanjolia, J. Vac. Sci. Technol. A **32**(1), 01A119 (2014). doi:10.1116/1.4843595. http://scitation.aip.org/content/avs/journal/jvsta/32/1/10.1116/1.4843595
9. G.E. Jellison, F.A. Modine, Appl. Phys. Lett. **69**(14), 2137 (1996). doi:10.1063/1.118155. http://scitation.aip.org/content/aip/journal/apl/69/14/10.1063/1.118155
10. M. Mews, T.F. Schulze, N. Mingirulli, L. Korte, Appl. Phys. Lett. **102**, 122106 (2013). doi:10.1063/1.4798292
11. R. Sinton, A. Cuevas, M. Stuckings, in *Proceedings of the 25th IEEE PVSC* pp. 457–460 (1996)
12. J.G. Choi, L. Thompson, Appl. Surf. Sci. **93**(2), 143 (1996). doi:10.1016/0169-4332(95)00317-7. http://www.sciencedirect.com/science/article/pii/0169433295003177
13. U. Das, S. Hegedus, L. Zhang, J. Appel, J. Rand, R. Birkmire, in *Photovoltaic Specialists Conference (PVSC), 2010 35th IEEE* (2010), pp. 001,358–001, 362. doi:10.1109/PVSC.2010.5614372
14. M.T. Greiner, L. Chai, M.G. Helander, W.M. Tang, Z.H. Lu, Adv. Funct. Mater. **22**(21), 4557 (2012). doi:10.1002/adfm.201200615